LRP 599/98 March 1998

Study of Second Stability Regime for ITG Modes in Tokamaks

M. Fivaz, O. Sauter, T.M. Tran,
J. Vaclavik, K. Appert

Submitted for Publication in
Physics of Plasmas

Study of second stability regime for ITG modes in tokamaks

M. Fivaz, O. Sauter, T. M. Tran, J. Vaclavik, K. Appert

Centre de Recherches en Physique des Plasmas - Association Euratom-Confédération Suisse - Ecole Polytechnique Fédérale de Lausanne, PPB, 1015 Lausanne, Switzerland.

Abstract

Ion-Temperature-Gradient (ITG) modes in tokamaks are stabilized when the plasma diamagnetism at high pressure reverses the magnetic drifts; this stabilization is studied in the trapped-ion and toroidal ITG regimes with a linear global gyrokinetic Particle-In-Cell code that uses the full MHD equilibrium data. It is found that a magnetic drift reversal parameter that scales like the gradient of the normalized pressure β describes the stabilization well, better than the standard ballooning parameter that scales like the Shafranov shift and poloidal pressure β_p. There exists a window of simultaneous second stability for MHD ballooning modes and ITG modes. Stability to global kink modes, in the presence of an ideal wall outside the plasma, is obtained for cases with high temperature gradients and with ITG growth rates that are an order of magnitude lower than at low plasma pressure.

I. Introduction

Ion-temperature-gradient-driven turbulence is commonly believed to cause strong anomalous radial energy transport in tokamak discharges and therefore to limit the performance of current and future tokamaks. Turbulence develops when the plasma equilibrium is linearly unstable; the knowledge of the stability conditions for ITG modes is therefore of great interest. In this paper, we discuss the stabilization of electrostatic ITG modes that occurs at high pressure, when the plasma diamagnetism creates a well in the magnetic field [1] [2] [3]. We show that this regime can be used to optimize the plasma stability simultaneously to ITG and MHD instabilities, for both short and long wavelengths.

The finite-pressure effects on electrostatic modes were studied numerically in Refs. [4] and [5] using the "$s-\alpha$" approximation to the equilibrium, which is valid at high aspect ratio for shifted circular magnetic surfaces. It was shown that increasing α, the radial derivative of the Shafranov shift, has a strong stabilizing effect on ITG modes; this is sometimes referred to as "Shafranov-shift stabilization". The same effect was seen in ref. [6] in a flux-conserving sequence of MHD equilibria. Analytical work related to the stabilization of trapped-ion modes can be found in Refs. [1] and [7]. The "$s-\alpha$" approximation to the equilibrium, however, is poor for the equilibria of typical tokamak plasmas, which are strongly shaped with a low aspect ratio. Moreover, these results were obtained using the ballooning approximation, which breaks down at low n or low magnetic shear, as the mode radial envelope varies over the distance between rational surfaces, and cannot describe slab-like modes that are not localized on the outer side of the torus, i.e. that do not "balloon". This approximation tends to break down in the most interesting cases. First, relatively low-n modes (trapped-ion modes) tend to produce the largest amount of anomalous ion heat transport. Second, we shall use low magnetic shear (though not very low) to stabilize the MHD ballooning modes at high pressure. Finally, we find modes that have a slab ITG character and do not "balloon".

We study this regime in detail with GYGLES (GYrokinetic Global Linear Electrostatic Solver) [3] [8], a fully-global linear gyrokinetic simulation code aimed at describing the most unstable ion-temperature-gradient modes in toroidal geometry. The code is based on a Particle-In-Cell method formulated with finite elements defined on magnetic coordinates, which has excellent numerical convergence properties. The poloidal mode

structure corresponding to $k_{||} = 0$ is extracted without approximation from the gyrokinetic equations. This results in a reduction of computing time by up to two orders of magnitude for a given resolution. The code can routinely simulate modes with both very long and very short toroidal wavelengths, can treat realistic (MHD) equilibria of any size, and runs efficiently on a massively parallel computer.

The previous results are therefore extended by the inclusion of global perturbations, necessary for an accurate description of trapped-ion modes, and of the MHD equilibrium data. We also use consistent MHD and kinetic equilibrium profiles and consider MHD stability, both in the regimes of high-n ballooning modes and low-n kink modes. However, we consider neither electromagnetic effects on the ITG modes nor the trapped-electron dynamics. Inclusion of the latter would permit the description of trapped-electrons modes; these where shown to be stabilized by drift-reversal in a study [9] of reversed-shear discharges where ITG modes were stable because of low η values. At high β, the electrostatic approximation that we use formally breaks down. We know from ballooning electromagnetic studies [5] [10] [11] [12], that further stabilization of the ITG modes can be expected when the perpendicular perturbation of the magnetic field is included in the model. However, the first finite-β effects on the eigenfrequency have been shown to come through the MHD equilibrium [6] [13] [14], which are modeled correctly. Inclusion of the parallel magnetic field perturbation could also lead to new instabilities in conditions close to magnetic drift reversal [7].

The remainder of this paper of organized as follows. Section II describes the gyrokinetic model we use and Sec. III the MHD equilibrium. We define a magnetic drift reversal parameter in Sec. IV and show its effect on gyrokinetic stability in Sec. V. In Sec. VI, we examine MHD stability and in Sec. VII the effects of shear and safety factor. We shown in Sec. VIII that the relevant regime can be obtained in experimental discharges and we conclude in Sec. IX.

II. Linear gyrokinetic model

Our model is based on the gyrokinetic equations for the ions, an adiabatic response for the electrons, the quasineutrality equation and the electrostatic approximation. This

unstable eigenmode. By analyzing the electrostatic potential and its time evolution, we can then compute the frequency, growth rate and spatial structure of the most unstable mode.

III. Consistent MHD equilibria

Any axisymmetric magnetic field can be written, using a cylindrical coordinate system (R, φ, Z):

$$\boldsymbol{B} = G\nabla\varphi + \nabla\Psi\times\nabla\varphi \tag{6}$$

The MHD equilibrium condition, or Grad-Shafranov equation, then reads [15]:

$$\nabla\cdot\frac{1}{R^2}\nabla\Psi = \frac{j_\varphi}{R} = -p' - \frac{GG'}{R^2} \tag{7}$$

where j_φ denotes the toroidal plasma current and the prime the derivative with respect to Ψ; G and p are free functions of Ψ that determine the equilibrium. We use consistent kinetic equilibrium distribution function f_0 and MHD equilibrium magnetic field: the pressure profile p is given straightforwardly by density and temperature profiles that determine f_0 in our gyrokinetic model:

$$p(s) = n_0(s)\left(T_e(s) + T_i(s)\right) \tag{8}$$

It is easier to choose the safety factor profile when G is specified implicitly by the surface averaged current density I^*:

$$I^*(s) = \frac{\oint j_\varphi \frac{J}{R} d\chi}{\oint \frac{J}{R} d\chi} \tag{9}$$

where $\oint d\chi$ denotes integration over the magnetic surface and J the appropriate Jacobian. The CHEASE code [16] solves the Grad-Shafranov equation for Ψ when I^*, p' and the plasma boundary are specified.

The full gyrokinetic stability problem is specified by four independent profiles: the density $n_0(s)$, the ion and electron temperatures $T_e(s)$ and $T_i(s)$ and the surface-averaged normalized current profile $I^*(s)$. Once these are chosen, the Grad-Shafranov equation is first solved (with CHEASE) using the profiles $I^*(s)$ and $p' = \frac{\mathrm{d}}{\mathrm{d}\Psi}p$ to determine $\Psi(R, Z)$ and $G(\Psi)$. The ITG stability is then obtained by solving the gyrokinetic equations, with

GYGLES, using the profiles $n_0(s)$, $T_i(s)$ and $T_e(s)$ and the magnetic field given by Ψ and G.

At fixed magnetic field, the density n_0 appears effectively only through its logarithmic gradient, which is insensitive to a multiplication by a constant. Equation (8), which couples the gyrokinetic problem to the Grad-Shafranov equation, introduces a new dependence of gyrokinetic stability on the absolute value of the density; the finite-pressure stabilization of ITG modes then occurs at high density.

IV. Magnetic drift reversal parameter α_t

At low normalized pressure β, the magnetic drifts are destabilizing on the outer side of the torus. If these drifts are reversed by the plasma diamagnetism at high pressure, they become stabilizing everywhere and lead [2] to what can be called a second stability regime for the ITG modes. A condition for drift reversal can be derived by noting that the unfavorable gradient occurs in the region where $\frac{\partial B}{\partial \psi} < 0$. Using the equation of MHD equilibrium $\mu_0 \nabla p = (\nabla \times \boldsymbol{B}) \times \boldsymbol{B}$, one can show that, for an axisymmetric system,

$$B\frac{\partial B}{\partial \Psi} = -\frac{1}{R}\frac{\partial R}{\partial \Psi}B_t^2 - \mu_0 \frac{\mathrm{d}p}{\mathrm{d}\Psi} + 0(B_p^2) \tag{10}$$

where B_t and B_p are the toroidal and poloidal components of the magnetic field. The $0(B_p^2)$ term on the right-hand side of this equation is small compared to the first one and may be neglected. Drift reversal thus occurs when, B_t being the toroidal magnetic field,

$$-\mu_0 \frac{\mathrm{d}p}{\mathrm{d}\psi} > \frac{1}{R}\frac{\partial R}{\partial \psi}B_t^2 \tag{11}$$

The pressure gradient must be sufficiently large to reverse the magnetic field gradient. Since large pressure gradients can destabilize MHD modes, configurations of practical interest have to be a compromise between microstability and MHD stability. We shall address this question later.

Locally on the outer plasma mid-plane, the drift reversal condition (11) can be rewritten in dimensionless form:

$$\alpha_t \equiv -\mu_0 \frac{R}{B_t^2}\frac{\partial p}{\partial R} = \frac{R}{2L_p}\beta^{loc} > 1 \tag{12}$$

with

$$\frac{1}{L_p} = -\frac{\partial}{\partial R} \ln p \quad \text{and} \quad \beta^{loc} = 2\frac{\mu_0 p}{B_t^2} \tag{13}$$

To quantify the magnetic field gradient reversal, it is natural to use the parameter α_t, which is equal to zero at low pressure and to one at full reversal on the outer mid-plane. It is therefore a local parameter characterizing the magnetic field gradient at the most unfavorable point. We note that a similar parameter

$$\alpha_p \equiv 2q^2\alpha_t \tag{14}$$

is the radial derivative of the Shafranov shift in the "$s - \alpha$" approximation of the equilibrium. It is often used to define the second stability zone for MHD ballooning modes and has been used in [4] and [5] to study ITG modes. It is usually called α; we use the notation α_p to recall that this parameter scales like the normalized poloidal plasma pressure β_p, unlike α_t which scales like the total pressure β.

V. Simultaneous second stability zone for MHD ballooning modes and ITG modes

Table (I) defines a set of equilibria with JET size and shape where:

- The normalized temperature gradient $R_0/L_T \equiv -\frac{R_0}{aT}\frac{\mathrm{d}T}{\mathrm{d}s}$ peaks at the magnetic surface $s = s_0$, and so confine the unstable modes around that surface. The maximum value (at $s = s_0 = 0.6$) can be varied by changing the parameter T_{mul}.
- The reversal parameter α_t at $s = s_0$ can be varied by changing the parameter j_0.
- In the region where the modes lie, the safety factor q does not depend on R_0/L_T and α_t, as is shown on Fig. (4).
- The magnetic shear $\hat{s}$ is low ($0 < \hat{s} < 0.2$) where the modes lie. This favors MHD stability and all these equilibria are in fact stable to MHD ballooning modes; in particular, equilibria with high pressure gradients lie in the second MHD stability zone.

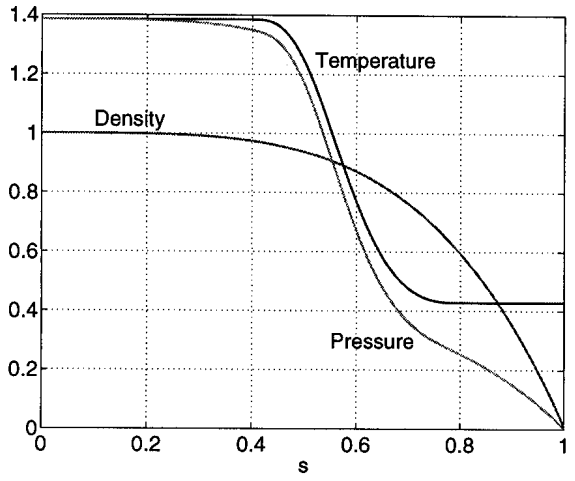

Figure 1: *Profiles from table (I), with T_{mul}=1.8 and j_0=1.5; normalized density, temperature and associated pressure.*

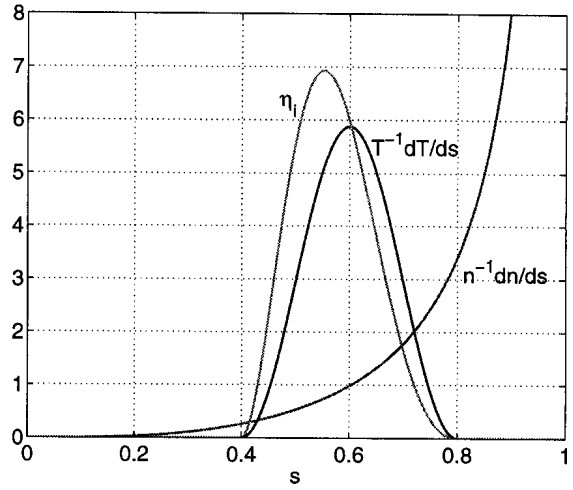

Figure 2: *Profiles from table (I), with T_{mul}=1.8 and j_0=1.5; logarithmic gradients of density $-\frac{n_i}{dn_i/ds}$, temperature $-\frac{T_i}{dT_i/ds}$, and corresponding value of η_i.*

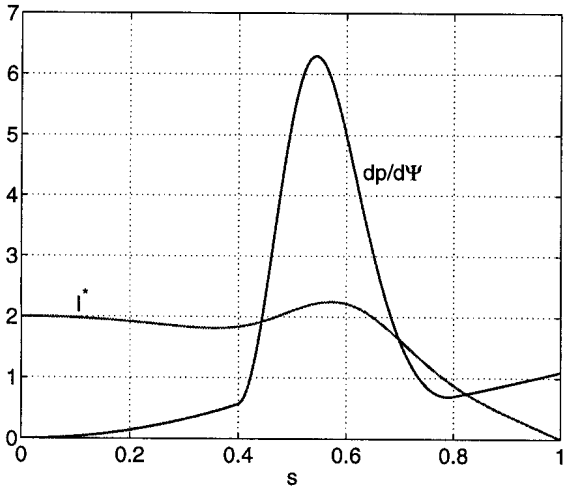

Figure 3: *Profiles from table (I), with T_{mul}=1.8 and j_0=1.5; current density I* and pressure gradient $-dp/d\Psi$, sources to the Grad-Shafranov Equation.*

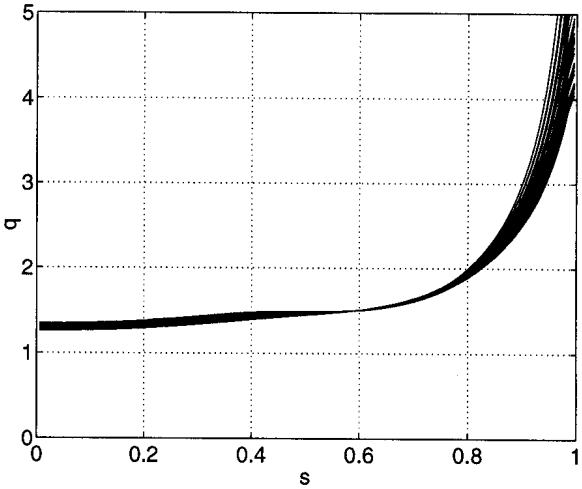

Figure 4: *Superposition of the safety factor profiles for all the equilibria studied which have $\alpha_t < 1.5$; since the unstable modes remain localized radially between $s = 0.4$ and $s = 0.8$, the relevant q profile is almost constant in the scan.*

Global parameters	Major radius $R_0 = 3$ m, aspect ratio $a/R_0 = 1/0.36$, elongation $\kappa = 1.6$, triangularity $\delta = 0.3$, $q_i/m_i = 4.8e7$ C/kg (deuterium)
Vacuum field at R_0	$B_0 = 3$ T
Safety factor at $s = s_0$	$q(s_0) = 1.5$
Ion temperature gradient	for $\|s - s_0\| < 2\Delta s$: $\frac{T_i}{dT_i/ds} = -\frac{1}{2}\kappa_T \left(1 + \cos\left[\frac{\pi}{2}\frac{s-s_0}{\Delta s}\right]\right)$
	for $\|s - s_0\| > 2\Delta s$: $\frac{T_i}{dT_i/ds} = 0$
	$\kappa_T = \frac{1}{\Delta s}\log(T_{mul})$, $s_0 = 0.6$, $\Delta s = 0.1$
	$T_i(s_0) \equiv T_0 = 10$ Kev
Electron temperature	$T_e(s) = T_i(s)$
Density profile	$n_i(s) = n_0(1 - s^2)^4$
Norm. pressure gradient	$\hat{p}' = \frac{1}{n_0 T_0}\frac{1}{2s}\frac{\mathrm{d}}{\mathrm{d}s} n_i T_i$
Norm. current profile	$\hat{I}^*(s) = j_0(1 - s^2) + j_a \exp\left[-\frac{(s-s_0)^2}{\Delta s_j^2}\right]$
	$j_a = T_{mul} * (.14 * j_0 + .24)$, $\Delta s_j = 0.15$
Scan parameters	$j_0 \in [0.8, 100]$, $T_{mul} \in [1.1, 1.8]$
Local parameters at $s = s_0$	$R_0/L_T \equiv \kappa_T R_0/a$, $R_0/L_n = 2.8$, shear $\hat{s} \approx 0.1$
	$\rho = 4.8$ mm, $\Omega \approx 144$ MHz, $\omega_b \approx 80$ kHz

Table I: *Specification of the JET-size equilibria studied. The temperature is of* 10 *keV at* $s = s_0$ *that steps up and down by a factor* T_{mul} *around this value over a fixed distance* Δs*; an example of the profiles obtained is given in Figs. (1)-(3). The values of* T_{mul} *and* j_0 *determine respectively the temperature gradient and the value of the reversal parameter* α_t*. The current profile is a parabola to which a local Gaussian current of amplitude* j_a *has been added around the maximum pressure gradient. The expression for* j_a *insures that the profiles of the safety factor and the magnetic shear are conserved during the scan. The normalized profiles* $\hat{p}'$ *and* $\hat{I}^*$ *are those given to the equilibrium code; their rescaled, final values are determined by the renormalization done by CHEASE to obtain the specified vacuum field at* $R = R_0$ *and safety factor at* $s = s_0$*.*

The equilibrium profiles obtained for $j_0 = 1.5$ and $T_{mul} = 1.8$ are shown in Figs. (1)-(3). The shape of the temperature profile closely resembles the experimental reversed shear discharge in the JT60-U tokamak from Ref. [17]. With this set, we perform a generic study of global ITG stability as a function of R_0/L_T and α_t at fixed safety factor profile, varying j_0 and T_{mul} only. In the text that follows, R_0/L_T and α_t refer to their values at $s = s_0$.

Figure (5) shows the ITG growth rate as a function of α_t for the $n = 48$ eigenmode. This mode is in the toroidal ITG regime as its frequency ω is larger than the trapped-ion bounce frequency $\omega_b \equiv \sqrt{\frac{as_0}{R_0}}\frac{1}{qR_0}\sqrt{\frac{T_i}{m_i}}$. As α_t is increased and the magnetic drifts are reduced, then reversed for $\alpha_t > 1$, the growth rate decreases until the mode is fully

stabilized. Strongly reversed drifts are needed to fully stabilize the modes.

For $n = 12$, the mode frequency ω is smaller than ω_b and the mode is in the trapped-ion regime. The effect of the drift reversal is qualitatively different, as shown in Fig. (6) by the solid line. As α_t is increased, the toroidal precession velocity of the trapped ions reduces, then reverses, completely stabilizing the trapped-ion mode for $\alpha_t > 1.2$. Small values of α_t ($\alpha_t < 0.5$) do not influence the growth rate (shown by the crosses) as much as in the toroidal ITG regime. For $\alpha_t > 1.2$, the growth rate of the trapped-ion mode lies below that of a coexisting slab-like ITG mode, and the frequency measured, being always that of the most unstable mode, jumps abruptly. This slab-like mode is close to marginal stability and remains weakly unstable, even at high values of α_t. Its slab-like nature is visible in its structure, Fig. (9d). Further evidence of the nature of the modes is obtained by artificially making all the particle passing (i.e. with constant $v_{||}$ and $v_\perp$), as in [3]; the trapped-ion mode then disappears, Fig. (6), dashed line, and the remaining slab mode, now weakly damped rather than weakly unstable, is seen for all values of α_t.

Figures (7) and (8) show the contours of the growth rates obtained for $n = 12$ and $n = 48$ in the (α_t,R_0/L_T) plane. The frequency of these modes increases with R_0/L_T and with n, whereas the ion bounce frequency ω_b is fixed. As a result, the $n = 12$ modes are in the trapped-ion regime ($\omega < \omega_b$), except at high R_0/L_T, where they have a small toroidal ITG character, and the $n = 48$ are in the toroidal ITG regime ($\omega > \omega_b$), except at very low values of R_0/L_T.

We call "first stability zone" for the ITG modes the stable zone that lies below the critical temperature gradient of $R_0/L_T \approx 4$. In the "second stability zone", at high values of α_t, the ITG modes are stabilized by ∇B reversal. The equilibria are fully stable in the toroidal ITG regime, while a weakly unstable slab-like mode remains in the trapped-ion regime. These slab-like modes are not expected to cause much anomalous transport, since they are radially narrow and only weakly unstable.

The structure of a few of the eigenmodes, marked (a) to (e) on Fig. (8), are shown in Figs. (9) and (10). The sequence (a)-(b) goes towards the boundary of the first stability zone, (a)-(c)-(d) towards the second stability and (a)-(c)-(e) follows approximately a line of constant growth rate. The mode (d) has a typical slab-like structure and is clearly different from the other eigenmodes shown.

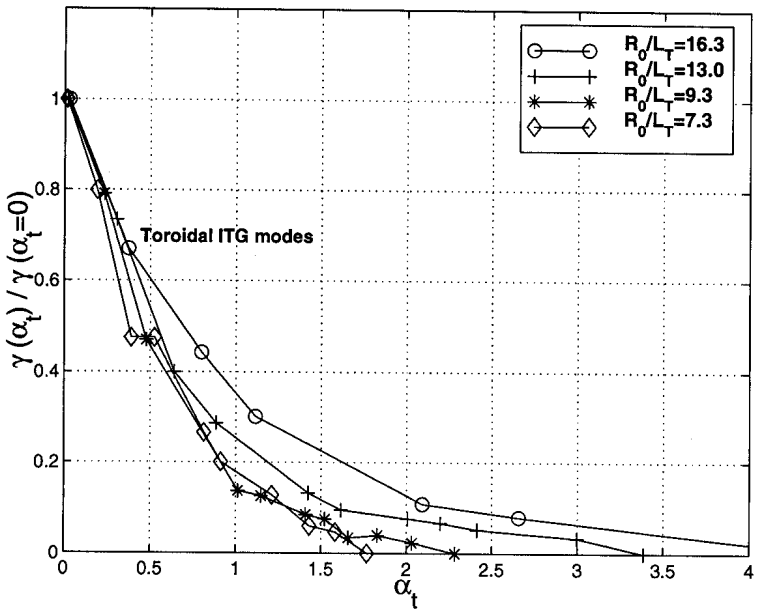

Figure 5: *Toroidal ITG regime, $n = 48$. Growth rate γ versus α_t for different temperature gradients. The growth rate is normalized to its value at $\alpha_t = 0$; stable modes are indicated by the arbitrary negative value of -0.1.*

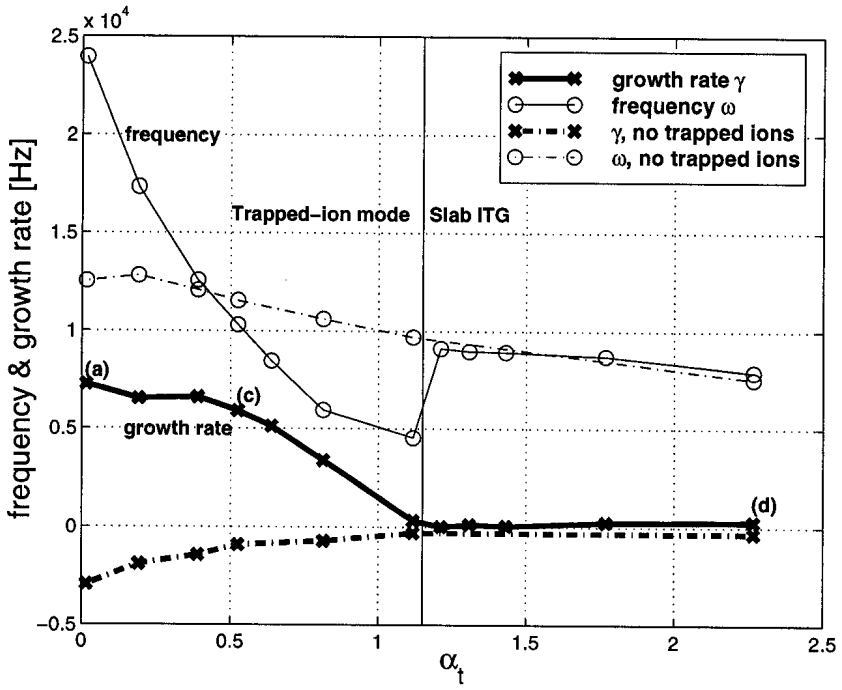

Figure 6: *Trapped-ion mode regime, $n = 12$. Frequency and growth rate as a function of α_t; the temperature gradient is $R_0/L_T = 7.3$. The corresponding mode structures are shown in Fig. (9) (a), (c) and (d). The mode at $\alpha_t = 0$ is of trapped-ion nature and is stable for $\alpha_t = 1.2$. At $\alpha_t = 1.2$, its growth rate goes below that of a coexisting slab-like ITG mode, and the frequency measured jumps abruptly to a new value. When all the ions are made artificially passing (dashed line) the trapped-ion mode disappear and we obtain the slab-like mode for all values of α_t.*

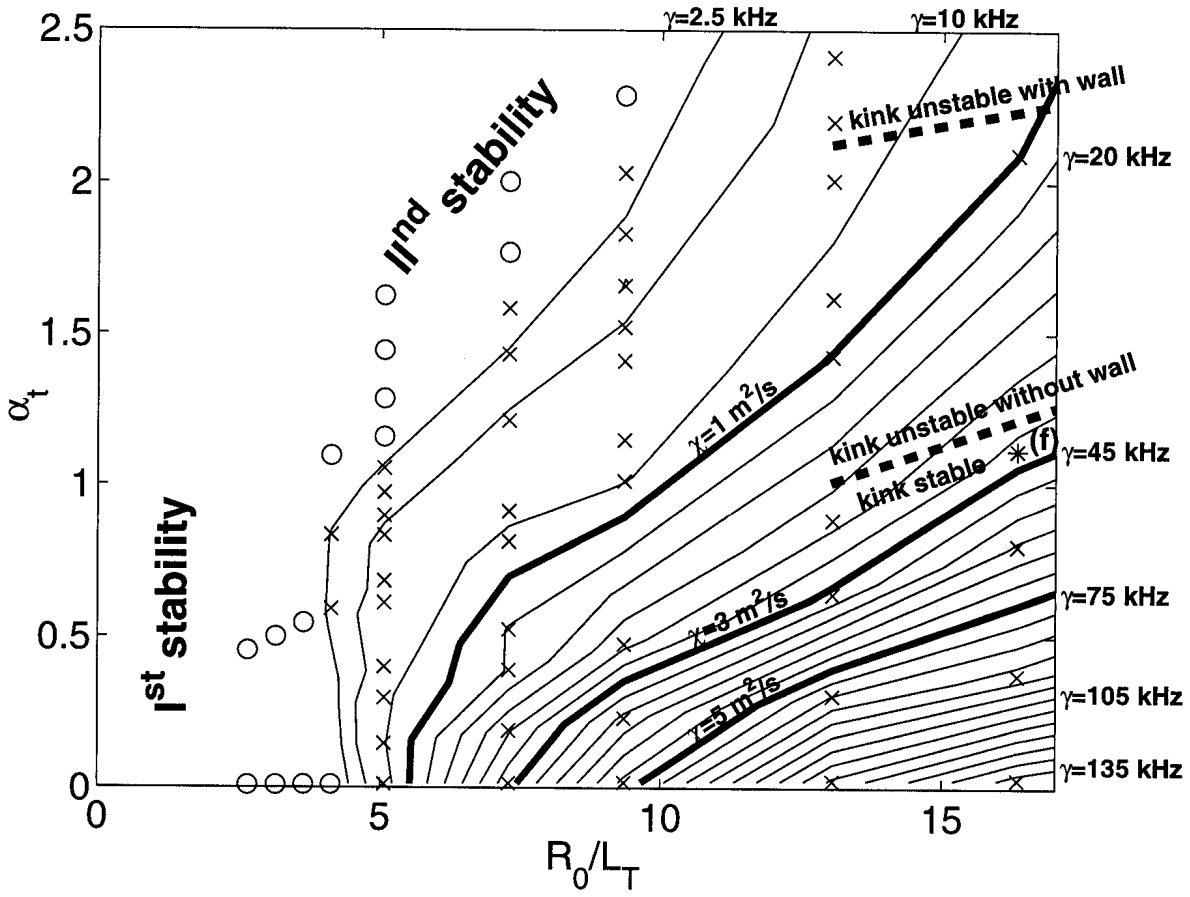

Figure 7: *Toroidal ITG regime. Contours of the growth rate for* $n = 48$ *versus* α_t *and temperature gradient* R_0/L_T. *The crosses (x) and circles (o) represent points where the equilibrium was found respectively unstable and stable. The* $n = 48$ *mode is in the toroidal ITG regime, except around* $R_0/L_T = 5$, *where the frequency is lower than the ion bounce frequency. It is quite sensitive to the magnetic field gradient and is fully stabilized above a* R_0/L_T*-dependent value of* α_t *which defines the boundary of the second stability zone. The eigenmode at point (f) is shown in Fig. (10).*

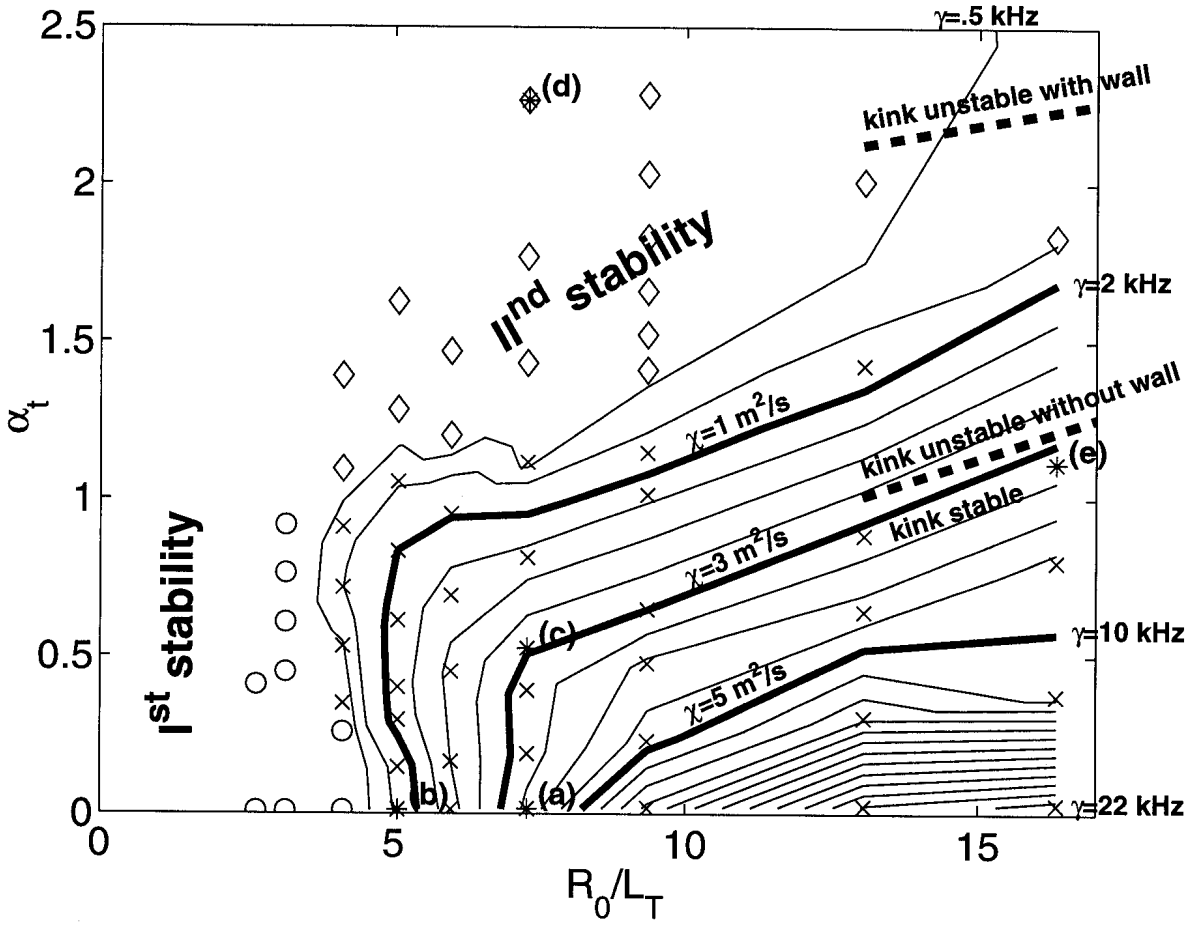

Figure 8: *Trapped-ion mode regime. Contours of the growth rate for* $n = 12$ *versus* α_t *and temperature gradient* R_0/L_T. *The circles (o) represent equilibria that are stable. The equilibria marked (◇) are very weakly unstable to slab-like ITG modes. Those marked (x) are unstable to trapped-ion modes; they are deep in the trapped-ion regime at low temperature gradient and have a small toroidal ITG character at higher gradient, because the frequency increases with* R_0/L_T. *The first stability zone lies at* $R_0/L_T \leq 4$ *while the second stability zone lies roughly above* $\alpha_t = 1.2$, *where the trapped-ion mode is stable, but a slab-like mode is very weakly unstable. The modes corresponding to the points (a) to (e) are shown in Figs. (9) and (10).*

The heat diffusivity coefficient $\chi_\perp$ induced by an unstable mode can be estimated roughly using mixing length arguments; we take here $\chi_\perp = \gamma/k_\perp^2$. As a function of n, $\chi_\perp$ is expected to peak roughly around $n = 12$, where $k_\theta \approx k_r$ (the poloidal and radial components of the wavevector). For $n = 12$, we take $k_\perp^2 = 2k_\theta^2$, with $k_\theta = 30\text{m}^{-1}$. For the $n = 48$ modes, $k_\theta > k_r$ and we take $k_\perp = k_\theta$, with $k_\theta = 120\text{m}^{-1}$. The contours of the growths rate corresponding to $\chi_\perp = 1$, 3 and 5 m^2/s are shown in bold in Figs. (7) and (8). While these values should not be taken as more than rough estimates, they show that the scan covers most of the experimentally relevant range of $0.1 - 10$ m^2/s.

We note that this second stable regime for ITG is different from the regime reported in [18], which is related to strong anisotropies in the equilibrium distribution function.

VI. MHD stability calculations

The CHEASE code was used to compute the stability of MHD ballooning modes. All the equilibria presented here are stable to these modes at the surface $s = s_0$; this was achieved by lowering the magnetic shear to a value around $\hat{s} \approx 0.1$, thus pushing the equilibria with high values of α_t into the second stability regime for ballooning modes [19].

Though the present scan was designed to study the dependence of stability on local plasma parameters, it is instructive to look at the global MHD stability limits. The code ERATO [20] was used to compute the stability to the ideal n=1 kink mode. We focus here on equilibria with R_0/L_T=16.3, the highest temperature gradient used in the scan. The stability boundary is shown with two dotted lines in Figs. (7) and (8); in the absence of a conducting wall outside the plasma, the kink mode is stable up to $\alpha_t = 1.2$ ($\beta_N \equiv \beta aB/I = 3.5$ [mT/MA]), where the ITG growth rates are already strongly reduced compared with their values at low α_t. In the presence of a perfectly conducting wall at r_{wall}/a=1.2, the kink mode is stable up to α_t=2.3 (β_N=5.4), which is in the second stability region for $n = 12$ and where the ITG growth rate for $n = 48$ is an order of magnitude lower than at α_t=0. The anomalous heat diffusivity is expected to be of the order of 1 m^2/s, a rather low value, although the temperature gradient is three times higher than the critical gradient (i.e. at α_t=0).

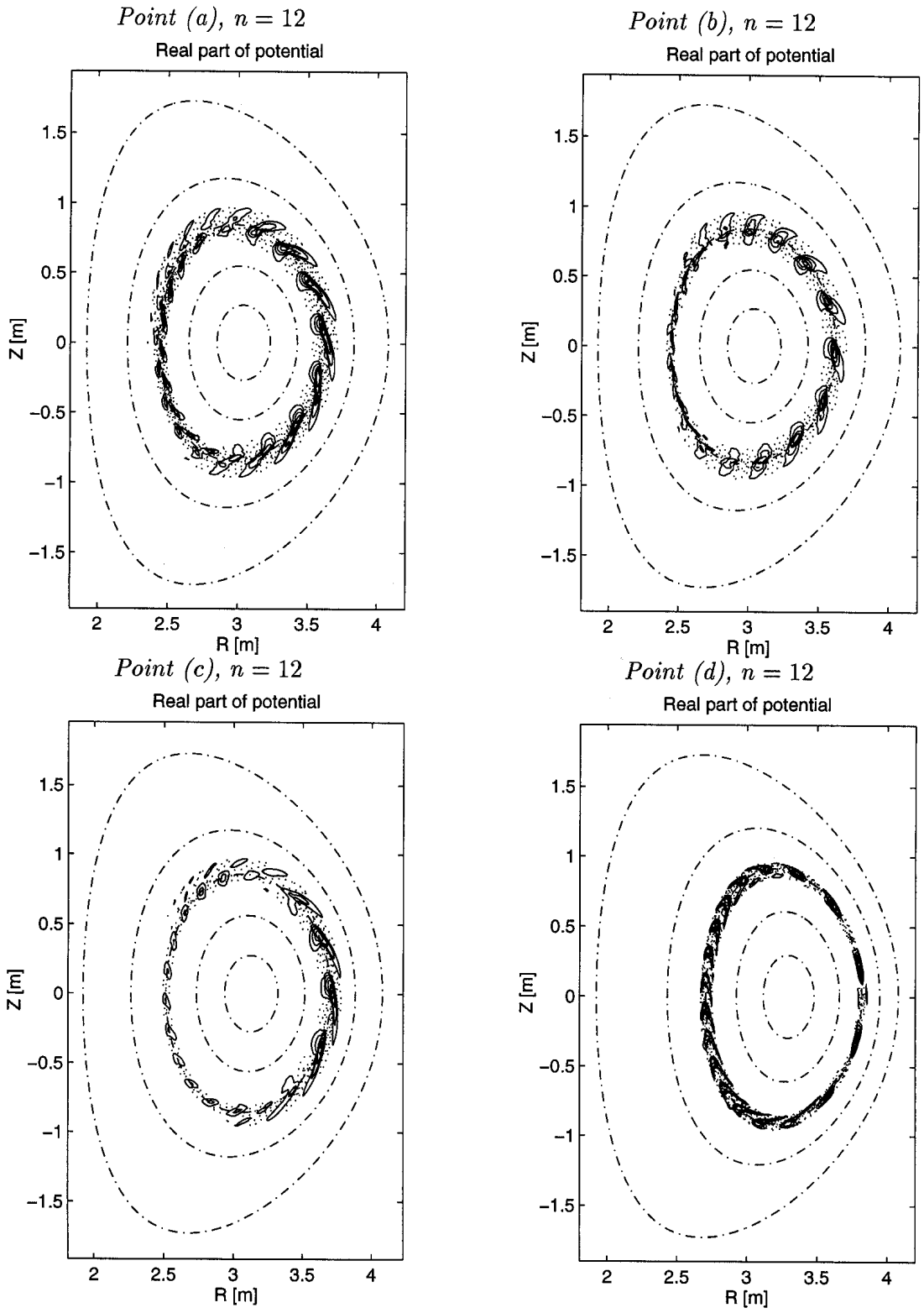

Figure 9: *Eigenmodes corresponding to the points (a)-(d) outlined in Figs. (6) and (8).*

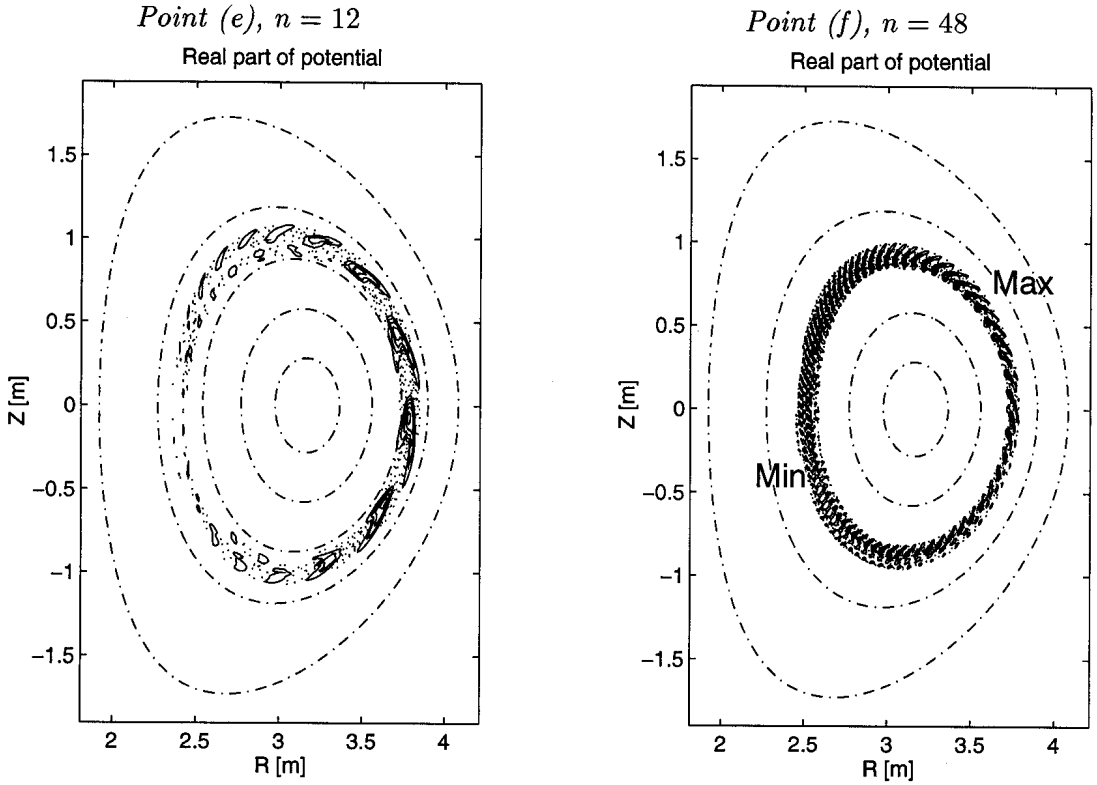

Figure 10: *Left: eigenmodes for* $n = 12$ *and* $n = 48$ *corresponding to the points (e) and (f) marked in Figs. (8) and (7). Right: the* $n = 48$ *eigenmode for the same equilibrium. It "balloons" around* $\theta = 60$ *degrees, where its maximum amplitude is three times larger than its minimum amplitude at* $\theta = 150$ *degrees.*

Optimization of the plasma shape and profiles could lead to even better configurations that are stable to all ideal MHD modes and stable or weakly unstable to global ITG modes. Further optimization could probably be obtained by allowing lower values for the aspect ratio.

VII. Effect of the safety factor

We now examine whether the second-stable regime for ITG modes is obtained at high α_t, as the drift-reversal condition indicates, or rather at high $\alpha_p \equiv 2q^2\alpha_t$, as for MHD ballooning modes. Figure (11) shows the growth rate versus α_t for different values of q at fixed $R_0/L_t = 7.3$. The value nq, which is proportional to the drift frequencies, is kept constant at $nq = 18$ in the scan, so that the mode frequency ω does not vary when q is changed. As the trapped-ion bounce frequency is inversely proportional to q,

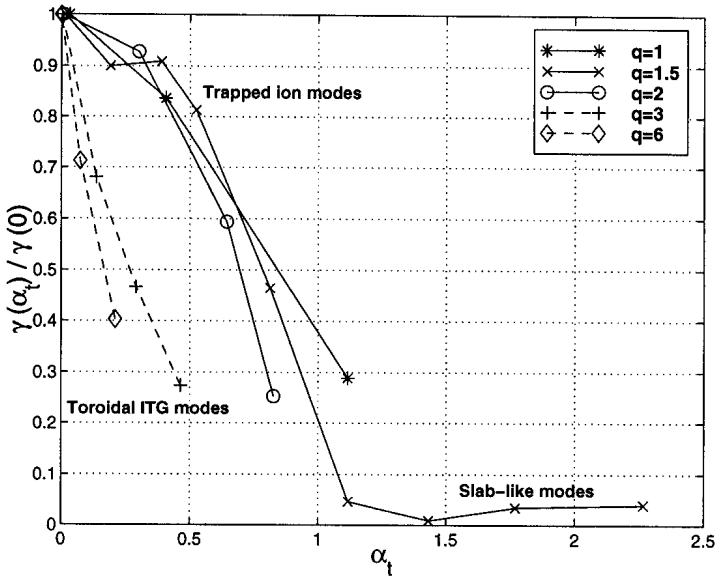

Figure 11: *Normalized growth rate versus* $\alpha \sim \beta/L_p$ *for different values of* q*; the quantity* $nq = 18$ *is kept constant in the scan. The equilibria are as in table (I) for fixed* $R_0/L_T = 7.3$*, except that the value of* q *is varied. The bounce frequency* $\omega_b \sim v_{thi}/qR_0$ *decreases when* q *is increased, so that the mode, whose frequency varies little, is in the trapped-ion regime for* $q < 2.5$ *and in the toroidal ITG regime for* $q > 2.5$*. This transition excepted, the accessibility to the second-stable regime does not depend much on* q *at constant* α_t*.*

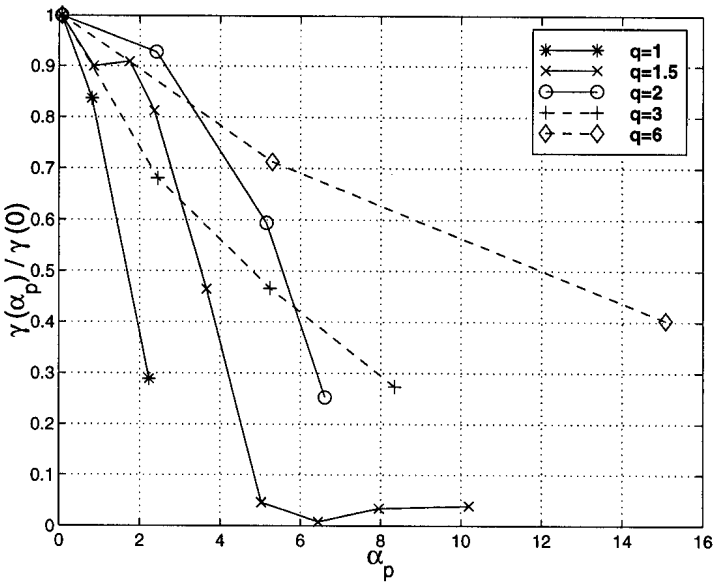

Figure 12: *Normalized growth rate from Fig. (11) replotted versus* $\alpha_p/2 = q^2\alpha_t$*. The values are scattered over a wide range in* α_p*; unlike for MHD ballooning modes, the finite-pressure stabilization for ITG modes is better described by* α_t *than by* α_p*, i.e. scales like* β/L_p *rather than* β_p/L_p*.*

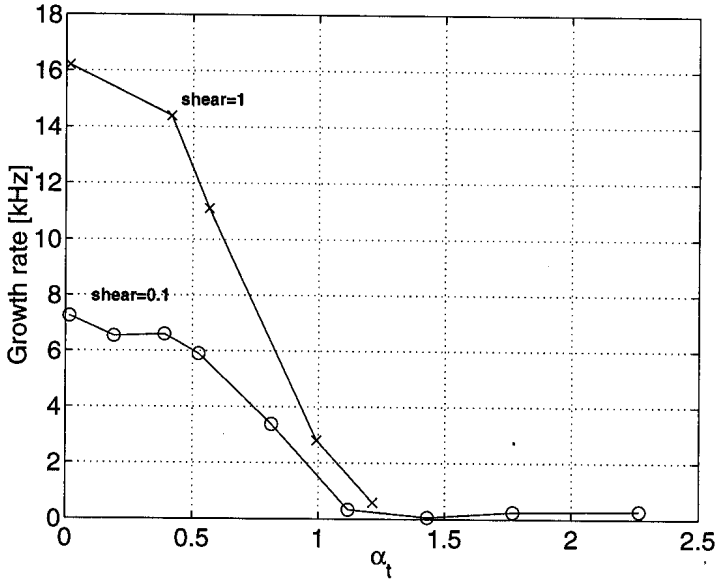

Figure 13: *Growth rate for the n=12 mode (trapped-ion mode) versus α_t for two different values of the magnetic shear. Low shear is stabilizing for α_t=0, but the drift-reversal stabilization occurs at the same value of α_t independently of the shear.*

the mode is in the toroidal ITG regime ($\omega_b < \omega$) for large values of q (here, $q > 2.5$) and in the trapped-ion regime ($\omega_b > \omega$) for low values ($q < 2.5$). These two regimes are reflected in the dependence of the growth rate on α_t, which decreases faster around $\alpha_t = 0$ for toroidal ITG modes, consistently with the results from Figs. (5) and (6). Within each of these regimes, the stabilization is well described by the parameter α_t. The same growth rates are shown versus α_p on Fig. (12); they are scattered over a wide range of α_p. The comparison with Fig. (11) shows that α_t describes the stabilization much better.

The magnetic shear $\hat{s}$ has a much stronger effect on the second stability limit for MHD ballooning modes than for ITG modes. In equilibria similar to those from table (I), but with higher shear, the equilibria become unstable to MHD ballooning modes for $\hat{s} \geq 0.5$. For ITG modes, higher shear increases the growth rates, however the marginal stability is still determined by α_t, and depends weakly on the shear, as seen in Fig. (13) for $\hat{s}$=0 and $\hat{s}$=1.

The access to the second-stable regime for the electrostatic ITG modes is not, unlike that for MHD ballooning modes, eased at low magnetic shear or high safety factor. It is better described by drift-reversal (large α_t, large β) than by a condition on the Shafranov

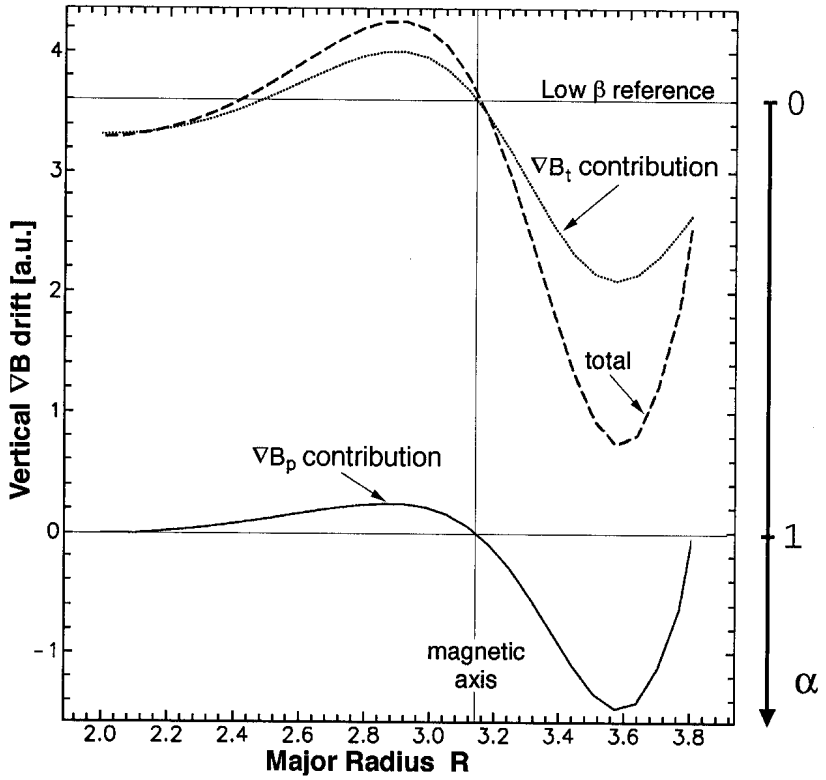

Figure 14: *Normalized vertical ∇B drift velocity from JET discharge number 38838. The data is obtained from the magnetic field reconstruction; the dashed line shows $\nabla B/B^2$ [a.u.], which is proportional to the ∇B drift velocity. Its value on the plasma midplane is plotted as a function of the major radius R. The full and dotted lines show respectively the contributions from the gradient of the poloidal and toroidal magnetic field. The low-β reference indicates the value obtained in a usual low-β discharge with $B \sim 1/R$. The drift velocity is reduced by a factor four at $R = 3.6$ compared to the usual low-β value, which corresponds to $\alpha = .75$.*

shift (large α_p, large β_p).

VIII. Discussion

We give here two examples where the favorable value of $\alpha \approx 1$ seems to have been obtained in experimental discharges. A reduction of ITG-induced transport is then expected. Of course, this can translate into improved confinement only if other transport mechanisms are not dominant.

Some reversed shear discharges [17] in the JT60-U tokamak show temperature profiles that are very similar to those used in our scan. There is an internal transport barrier

where the pressure gradient is very steep and the confinement very good; a rough estimate from the published data indicates that α_t is of the order of one. We note that the control of MHD instabilities is critical to obtain such discharges.

An analysis of a small number of JET discharges has shown that $\alpha_t \approx .75$ has been obtained. Discharge number 38838 has $\beta = 3\%$, $\beta_p = 1.5$, a current I=1 MA and a magnetic field B=1 T. The quantity $\nabla B/B^2$ on the plasma midplane, which is proportional to the vertical ∇B drift and to (1-α_t), was computed from the reconstructed equilibrium and shown in Fig. (14). It is reduced by a factor of four compared to the value obtained in a usual, low-β configuration with $B \sim 1/R$ and $\alpha_t = 0$. The corresponding value of α_t is larger than 0.5 over half of the small radius and peaks at $\alpha_t = 0.75$ for $R = 3.6$. The global confinement time was not better than for a typical JET H mode, but the reduction of ITG-induced transport might have been masked by other transport mechanisms; the discharge has MHD activity and the density approaches the Greenwald limit, which can degrade the confinement.

IX. Conclusions

Similarly to MHD ballooning modes in the second stability regime, ITG modes are stabilized at high pressure gradient, when the plasma diamagnetism reverses the magnetic drifts. This stabilization is well described in general axisymmetric equilibria by the reversal parameter:

$$\alpha_t = -\mu_0 \frac{R}{B^2} \frac{\partial p}{\partial R} = \frac{R}{2L_p} \beta^{loc}$$

We have shown that the ITG modes are stabilized at high values of α_t, and that these values are roughly independent of the safety factor and the magnetic shear; α_t describes the stabilization better than the standard ballooning parameter α_p that scales like the Shafranov shift and β_p. The trapped-ion modes (low n) are fully stabilized for $\alpha_t \geq 1.2$; the toroidal ITG modes (high n) are more affected by small values of α_t, but higher values are often required for full stabilization. Electromagnetic effects and trapped-electron dynamics should be included to confirm these results and obtain quantitative thresholds; this should be the main emphasis in the near future.

The stabilization occurs at high values of the pressure gradient, which tend to destabi-

lize MHD modes; a regime of simultaneous second stability for ITG modes and MHD ballooning modes has been found at low magnetic shear. Stability to global ($n = 1$) kink modes is helped by an ideal wall; in that case, we have found kink-stable configurations at $\beta_N = 5.4$ with temperature gradients three times above the low-β critical gradient, where trapped ion modes are stable and toroidal ITG have growth rate that are an order of magnitude lower than for α_t=0.

Further simultaneous optimization for ITG and MHD stability should be possible by modifying the profiles, plasma shape and aspect ratio; the latter was set in this paper around the value for conventional tokamaks. Values of α_t of unity are expected to reduce strongly any ITG-induced transport. Such values are attainable in practical discharges, as shown with examples from the JET and JT60U tokamaks.

Aknowlegements

This research was supported in part by both the Cray/EPFL (Ecole Polytechnique Fédérale in Lausanne) Parallel Application Technology Program and the Swiss National Science Foundation. The computations have been performed on the Cray-T3D of the EPFL. We thank S. Brunner, S. Parker and R. Sydora for useful discussions.

References

[1] M. Rosenbluth and M. L. Sloan, Phys. Fluids **14**, 1725 (1971).

[2] M. Fivaz, T. Tran, K. Appert, J. Vaclavik, and S. E. Parker, Phys. Rev. Lett. **78**, 3471 (1997).

[3] M. Fivaz, Ph.D. thesis, Ecole polytechnique Fédérale de Lausanne, Switzerland, thesis 1692, 1997.

[4] X. Q. Xu and N. M. Rosenbluth, Phys. Fluids B **3**, 627 (1991).

[5] M. Yamagiwa, A. Hirose, and M. Elia, Plasma Phys. Control. Fusion **39**, 531 (1997).

[6] G. Rewoldt, W. M. Tang, and M. S. Chance, Phys. Fluids **25**, 480 (1982).

[7] X. Q. Xu and M. N. Rosenbluth, Phys. Fluids B **3**, 1807 (1991).

[8] M. Fivaz, S. Brunner, G. de Ridder, O. Sauter, T. M. Tran, J. Vaclavik, L. Villard, and K. Appert, to appear in Computer Physics Communications (1998).

[9] M. A. Beer, G. W. Hammett, G. Rewoldt, E. J. Synakowski, M. C. Zarnstoff, and W. Dorland, Phys. Plasmas **4**, 1792 (1997).

[10] J. Y. Kim, W. Horton, and J. Q. Dong, Phys. Fluids B **5**, 4030 (1993).

[11] R. R. Domingez and R. W. Moore, Nucl. Fusion **26**, 85 (1986).

[12] A. Jarmen, P. Anderson, and J. Weiland, Nucl. Fusion **27**, 941 (1987).

[13] G. Rewoldt, W. M. Tang, and R. J. Hastie, Phys. Fluids **30**, 807 (1987).

[14] G. Rewoldt, W. M. Tang, S. Kaye, and J. Menard, Phys. Plasmas **3**, 1667 (1996).

[15] V. D. Shafranov, Sov. Phys. JETP **8**, 494 (1958).

[16] H. Lütjens, A. Bondeson, and O. Sauter, Comput. Phys. Commun. **97**, 219 (1996).

[17] Y. Neyatani and the JT60-Team, Plas. Phys. Control. Fusion **38**, A181 (1996).

[18] H. Song, A. K. Sen, and G. Rewoldt, Phys. plasmas **3**, 4568 (1996).

[19] D. Lortz and J. Nührenberg, Phys. Lett. **68A**, 49 (1978).

[20] R. Gruber, F. Troyon, D. Berger, L. C. Bernard, S. Rousset, R. Schreiber, W. Kerner, W. Schneider, and K. V. Roberts, Comput. Phys. Commun. **21**, 323 (1981).